Global oceanic iron distribution estimated by dynamic interpolation

Toshimasa Doi[1], Satoshi Osafune[1], Shuhei Masuda[1], Hajime Obata[2], Kazuhiro Misumi[3], Eric Pieter Achterberg[4], Andrew Bowie[5], and Jun Nishioka[6]

[1]Japan Agency for Marine-Earth Science and Technology
[2]Atmosphere and Ocean Research Institute, The University of Tokyo
[3]Central Research Institute of Electric
[4]GEOMAR Helmholtz Centre for Ocean Research Kiel,
[5]University of Tasmania
[6]Hokkaido University

November 21, 2022

Abstract

The availability of dissolved iron (dFe) exerts an important control on primary production. Recent ocean observation programs have provided information on dFe in many parts of the ocean, but knowledge is still limited concerning the rates of processes that control the concentrations and cycling of dFe in the ocean and hence the role of dFe as a determinant of global primary production. We constructed a three-dimensional gridded dataset of oceanic dFe concentrations by using both observations and a simple model of the iron cycle, and estimated the difference of processes among the ocean basins in controlling the dFe distributions. A Green's function approach was used to integrate the observations and the model. The reproduced three-dimensional dFe distribution indicated that iron influx from aeolian dust and from shelf sediment were 7.6 Gmol yr and 4.4 Gmol yr in the Atlantic Ocean and 0.4 Gmol yr and 4.1 Gmol yr in the Pacific Ocean. The residence times were estimated to be 12.2 years in the Atlantic and 80.4 years in the Pacific. These estimates imply large differences in the cycling of dFe between the two ocean basins that would need to be taken into consideration when projecting future iron biogeochemical cycling under different climate change scenarios. Although there is some uncertainty in our estimates, global estimates of iron cycle characteristics based on this approach can be expected to enhance our understanding of the material cycle and hence of the current and future rates of marine primary production.

Global oceanic iron distribution estimated by dynamic interpolation

Toshimasa Doi[1], Satoshi Osafune[1], Shuhei Masuda[1], Hajime Obata[2], Kazuhiro Misumi[3], Jun Nishioka[4], Eric P. Achterberg[5], and Andrew Bowie[6]

[1]Global Ocean Observation Research Center, Research Institute for Global Change, Japan Agency for Marine-Earth Science and Technology (JAMSTEC), Yokosuka, Kanagawa, 237-0061, Japan.

[2]Atmosphere and Ocean Research Institute, the University of Tokyo, Kashiwa, Japan.

[3]Environmental Science Research Laboratory, Central Research Institute of Electric Power Industry, Chiba, Japan.

[4]Pan-Okhotsk Research Center, Institute of Low Temperature Science, Hokkaido University, Sapporo, Japan.

[5]GEOMAR Helmholtz Center for Ocean Research Kiel, Kiel, Germany.

[6]Antarctic Climate and Ecosystems CRC and Institute for Marine and Antarctic Studies, University of Tasmania, Hobart, Tasmania 7001, Australia.

Corresponding author: Toshimasa Doi (doit@jamstec.go.jp)

Key Points:

- A three-dimensional dissolved-iron dataset of the global ocean was constructed.
- Parameters of iron-cycle processes were optimized via a Green's function approach.
- A large differences in iron-cycle processes among the basins were represented by the data synthesis of the observations.

Abstract

The availability of dissolved iron (*dFe*) exerts an important control on primary production. Recent ocean observation programs have provided information on *dFe* in many parts of the ocean, but knowledge is still limited concerning the rates of processes that control the concentrations and cycling of *dFe* in the ocean and hence the role of *dFe* as a determinant of global primary production. We constructed a three-dimensional gridded dataset of oceanic *dFe* concentrations by using both observations and a simple model of the iron cycle, and estimated the difference of processes among the ocean basins in controlling the *dFe* distributions. A Green's function approach was used to integrate the observations and the model. The reproduced three-dimensional *dFe* distribution indicated that iron influx from aeolian dust and from shelf sediment were 7.6 Gmol yr^{-1} and 4.4 Gmol yr^{-1} in the Atlantic Ocean and 0.4 Gmol yr^{-1} and 4.1 Gmol yr^{-1} in the Pacific Ocean. The residence times were estimated to be 12.2 years in the Atlantic and 80.4 years in the Pacific. These estimates imply large differences in the cycling of *dFe* between the two ocean basins that would need to be taken into consideration when projecting future iron biogeochemical cycling under different climate change scenarios. Although there is some uncertainty in our estimates, global estimates of iron cycle characteristics based on this approach can be expected to enhance our understanding of the material cycle and hence of the current and future rates of marine primary production.

Index Terms: 0489, 4273, 4260, 4805, 4866

Keywords: global ocean, oceanic dissolved iron, iron cycle, data synthesis

1. Introduction

Iron is known to be an essential element for phytoplankton growth, and a reduced availability of dissolved iron (*dFe*) in the ocean has been shown to limit primary production rates in the Southern Ocean, Pacific equatorial upwelling system, and parts of the subarctic Pacific. It has been challenging, however, to document the global distribution of *dFe* in the ocean since concentrations are very low making accurate measurements challenging (e.g., Bowie & Lohan, 2009). For that reason, neither the biogeochemical cycle of the iron nor its distribution have been fully understood and hence this is still an active research topic internationally (e.g., Blain & Tagliabue, 2016).

Progress has been made over the last decades in trace metal sampling and measurement techniques, and the number of observations of *dFe* in seawater has increased rapidly. In particular, the international program “GEOTRACES” has been promoting observations and data sharing through its Intermediate Data Products, the most recent being released in 2017 (Schlitzer et al., 2018). Thanks to such efforts, it has become possible to discern the distribution of *dFe* on the basin scale along observational sections. However, in many regions of the World's ocean there are remain no *dFe* observations, making it difficult to grasp the overall picture of the global iron distribution.

To study biogeochemical cycles in the ocean, use has been made of material cycle models that combine physical and biogeochemical processes with a focus on elements such as carbon, nitrogen, and oxygen (e.g., Schmittner et al., 2008). Lower-trophic-level ecosystem models have been used effectively to assess ocean primary production, and the importance of taking into account the influence of *dFe* in the modeling of phytoplankton primary production is commonly recognized (Aumont et al., 2015; Resing et al., 2015). The development of these material cycle models have allowed modeling studies of *dFe* dynamics in the ocean to become more sophisticated. Improved understanding of the dynamics of *dFe* in the ocean has implicated the importance of physical and biogeochemical processes (e.g., Archer & Johnson, 1999; Aumont & Bopp, 2006; Doney et al., 2006; Gregg et al., 2003; Misumi et al., 2011; Moore & Braucher, 2008). Moore and Braucher (2008) and Misumi et al. (2014) have advanced understanding of the iron cycle on a basin scale with the use of a detailed lower-trophic-level ecosystem model containing a *dFe* compartment. Misumi et al. (2011) have clarified through analysis of their iron cycle model that estimation of the fate of iron that originates from shelf sediment is important in the North Pacific. Tagliabue et al. (2016) have summarized the performance comparison of several models. They report that various processes associated with the iron cycle have been proposed, and they discuss how well these processes do in replicating the observed distribution of iron. There remains a need to quantitatively define the importance of these processes, and analyses have revealed large ambiguities in inputs of iron from dissolution of aeolian dust (Luo et al., 2003), from shelf sediment (e.g., Moore et al., 2004), and from hydrothermal plumes (Tagliabue et al., 2010). In recent model studies, these inputs are given as forcing variables. Frants et al. (2016) used an inverse method to constrain an iron cycle model to the observational data and estimated the source and sink distribution of *dFe* and biogeochemical parameters. From the estimated results of them, the importance of iron supply from hydrothermal plumes was discussed along with aeolian iron and iron supplied from sediment.

The aim of our study was to obtain new insights into the global ocean lower-trophic-level ecosystem by taking into account a realistic distribution of *dFe*. The first step of this effort was construction of a useful, gridded, three-dimensional *dFe* distribution by applying a data

assimilation approach. The available *dFe* observations were assimilated to a global circulation model by using a Green's function (Menemenlis et al., 2005). The obtained gridded *dFe* data were spatiotemporally interpolated data with a dynamical consistency. We describe the numerical model that we used, the observational data, and the method of data synthesis used to assimilate results of estimated iron distributions. We discuss differences between ocean basins and conclude with a discussion of future approaches.

2. Methods

2.1 Model Description

We used a simplified oceanic iron cycle model that included advection and diffusion as well as sources and sinks of oceanic iron (Figure 1). The temporal rate of change of the concentration of *dFe* was represented by two physical processes, advection (*ADV*) and diffusion (*DIFF*), and by source-minus-sink processes (*SMS*), as shown in equation (1),

$$\frac{\partial dFe}{\partial t} = ADV(dFe) + DIFF(dFe) + SMS(dFe) \tag{1}$$

The units of *dFe* are nmol L^{-1}. The *ADV* and *DIFF* includes horizontal and vertical components, respectively. The iron cycle processes except to the advection and diffusion, *SMS*(*dFe*), are shown in Figure 1 and were drawn based on Moore and Braucher (2008) and Tagliabue et al. (2017). As the external sources of iron to the ocean, atmospheric dust that is deposited into the surface ocean and iron release from shelf sediments were considered.

The dust supply from the atmosphere was taken from the Modern-Era Retrospective analysis for Research and Applications, Version 2 (MERRA-2) (Gelaro et al., 2017). The monthly mean dust fluxes averaged over the 10-year period from 1980 to 1989 were used as the climatological dust fluxes at the sea surface. Five categories of dust particle sizes are defined in MERRA-2. To simplify the model, the concentrations of dust in these categories were merged, and the total concentrations were used in the model. Moreover, the dry and wet dust deposition in MERRA-2 were combined as the total dust deposition. Figure 2 shows the horizontal distribution of the annual mean values of the calculated dust deposition. Following Moore et al. (2004), we assumed that the dust contained a constant percentage of 3.5% iron by weight, and that 2% of the iron dissolved instantaneously at the sea surface.

The iron flux from seafloor sediments was set to a constant supply rate. This iron flux was hypothesized to be the source of iron from shelf sediments. Because of the coarse model grid, the seafloor to a depth of 1000 m was assumed to be the shelf. In the water column, settling particles of dust and organic matter were taken into account, and the processes of iron

dissolution and iron scavenging associated with the particles were parameterized. Following Moore and Braucher (2008), the scavenging process was estimated as a function of the *dFe* concentration as follows:

$$scav = Sc \times dFe \tag{2}$$

$$Sc = Sc_b \qquad (dFe < LC) \tag{3}$$

$$Sc = Sc_b + (dFe - LC) \times C_{high} \qquad (dFe \geq LC) \tag{4}$$

$$Sc_b = Sc_p \times POC + Sc_d \times Dust \tag{5}$$

where *scav* is the amount of *dFe* scavenging, *Sc* is the scavenging rate, Sc_b is the standard scavenging rate, *LC* is the ligand concentration, C_{high} is a proportionality constant, *POC* is the concentration of particulate organic carbon, and *Dust* is the concentration of dust particles. Sc_p and Sc_d are the scavenging rates for *POC* and *Dust*, respectively. For iron dissolution from particles, we assumed a constant rate of iron supply as follows:

$$Ds_p = Rd_p \times Fe_p \tag{6}$$

$$Ds_d = Rd_d \times Fe_d \tag{7}$$

where *Ds* is the amount of dissolution from particles, *Rd* is the dissolution rate, and *Fe* is the iron concentration contained in particles. The suffixes p and d indicate *POC* and *Dust*, respectively. The process of iron dissolution from organic particles is described by a single parameter, which accounts for the reduction of *Fe* via decomposition by biological activity and desorption from particles.

The consumption of *dFe* was parameterized as uptake by phytoplankton as follows:

$$Cs = v_{chl} \times C_{chl} \tag{8}$$

where *Cs* is the amount of *dFe* consumed by phytoplankton, v_{chl} is the consumption rate, and C_{chl} is the biomass of phytoplankton expressed in terms of the chlorophyll-*a* concentration. We used SeaWiFS climatological monthly mean chlorophyll-*a* data (McClain et al., 1998) as metrics of the concentration of phytoplankton at the sea surface. We assumed that the phytoplankton concentration decreases linearly with depth from the sea surface to zero at a depth of 250 m. Although this assumption does not take into account subsurface chlorophyll maxima in the subtropics, our model gave priority to simplicity. Because of the assumption that the iron absorbed by phytoplankton becomes associated with POC through the mortality of phytoplankton and the grazing or excretion by zooplankton, the iron consumed by phytoplankton was added to the iron included in the POC.

As with the chlorophyll-*a* data, SeaWiFS climatological monthly mean POC data were used as metrics of the POC concentrations at the sea surface. The spatial distribution was estimated by extending the surface values to subsurface depths on the assumption that the POC concentration decreased as a power function of depth: $(z/100)^{-0.858}$, where z is depth (m). This form was the expression of the vertical profile of the POC flux estimated by Martin (1987) using the POM flux obtained from the sediment trap.

We only include and focused on aeolian dust and shelf sediments as the sources of iron in this study, which recognizing that hydrothermal plumes on the seafloor and sea ice around the polar region may not be negligible sources of *dFe* (Bennett et al., 2008; German et al., 2016; Smith et al., 2007). As the first task of the assimilating observed iron in the global ocean, we sought to explain the observed *dFe* distribution by using three-dimensional gridded *dFe* data estimated from the simple oceanic iron cycle model shown in Figure 1.

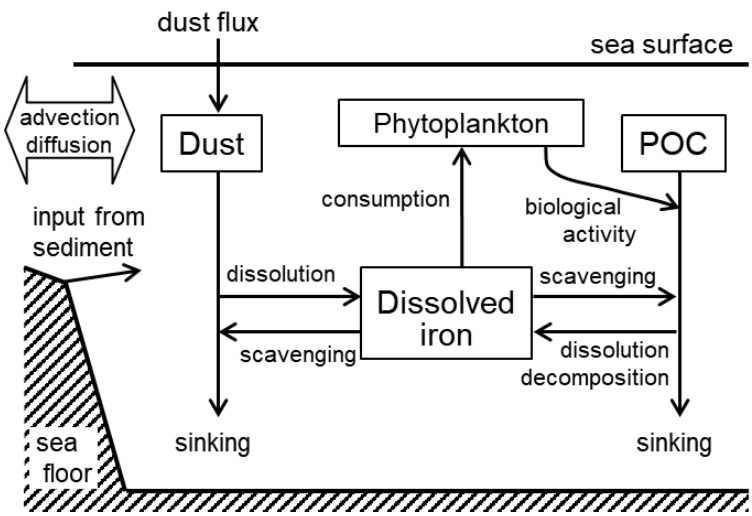

Figure 1. Schematic view of the simplified iron cycle model.

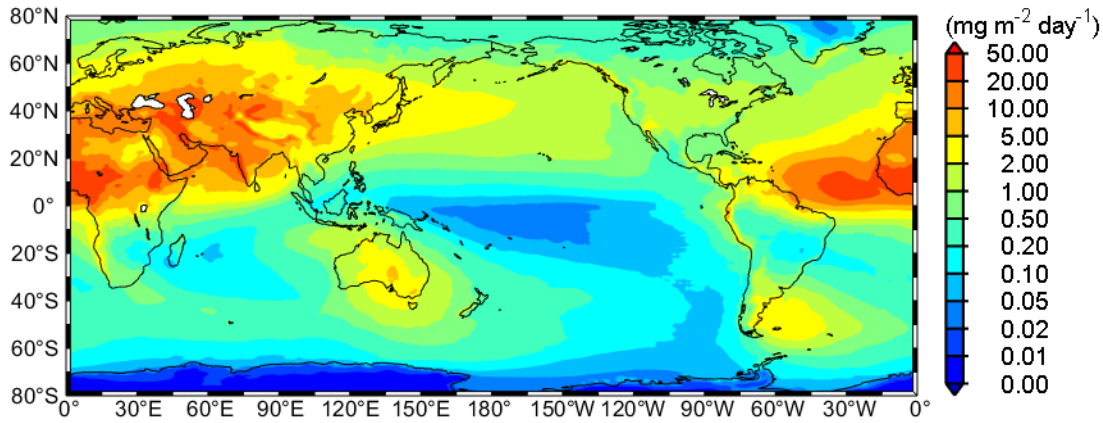

Figure 2. Annual mean dust deposition taken from MERRA-2 data.

For the physical process of iron transport, the advection/diffusion model was used along with the ESTOC (Estimated State of Global Ocean for Climate Research) flow field that is published on the JAMSTEC web site. This dynamical ocean state (flow field, temperature, and salinity) was constructed from a long-term ocean state estimation derived by four-dimensional variational data assimilation of physical components. This synthesis system was used with an ocean general circulation model (OGCM), version 3 of the Modular Ocean Model (MOM3) of the US Geophysical Fluid Dynamics Laboratory (Pacanowski and Griffies, 1999), with major model parameter values optimized to better reproduce the deep-water masses and thus the abyssal circulation (Kouketsu et al., 2011; Masuda et al., 2010; Osafune et al., 2015; Toyoda et al., 2015). This model covers the global ocean basin from 75˚S to 80˚N and the full depth range. The horizontal resolution of both latitude and longitude is 1°, and there are 45 vertical levels.

The 1980 ESTOC flow field was used to specify the physical conditions for the offline model. Since mean states of ESTOC flow fields have inevitable biases such as those related to parameterizations of subgrid processes, an initial shock caused by an attempt to eliminate the biases forcibly may include. To avoid such biases, we chose the mean state in 1980, which is around the midpoint of the ESTOC assimilation window. The monthly mean ESTOC flow field in 1980 was temporally interpolated at the model time step, and the annual flow field was applied cyclically at the time steps of the iron cycle model.

2.2 Observational data

In this study, we used three *dFe* observational databases to optimize the model parameters: the data contained in the GEOTRACES Intermediate Data Product 2017 (GEOTRACES IDP2017) Version 2 (Schlitzer et al., 2018), the historical data compiled by Moore & Braucher (2008) and Tagliabue et al. (2012), and the more recent reported data in the North Pacific Ocean by Yamashita et al. (2020) and Nishioka et al. (2020). The GEOTRACES IDP2017 covers *dFe* data in Atlantic Ocean sections (GA03: Fitzsimmons et al., 2015; Hatta et al., 2014; GA02: Rijkenberg et al., 2014; GAc01: Saito et al., 2013), Arctic Ocean sections (GIPY11: Klunder et al., 2012a and b), Indian Ocean section (GI04: Nishioka et al., 2013; Vu & Sohrin, 2013), Pacific Ocean sections (GP02: Nishioka & Obata, 2017; Zheng et al., 2017; GP18: Minami et al., 2015; GP16: Boiteau et al., 2016; Fitzsimmons, et al., 2017; Heller, et al., 2017; John et al., 2018; Resing et al., 2015; Sanial et al., 2018; GP13: Ellwood et al, 2018), and Southern Ocean sections (GIPY06: Bowie et al., unpublished, Tagliabue et al., 2012; GA10; GIPY04: Abadie et al., 2017; Chever et al., 2010; Lacan et al., 2008; GIPY05: Klunder et al., 2011 and 2013). The GEOTRACES database includes quality check flags. We used ‘good’ data that were flagged as ‘1’. These data were arranged in 45 layers on a 1° grid. After removal of duplicate data, the data in each grid were averaged. We used this merged

observational *dFe* concentration data as the climatological data (Figure 3). The data set covered the Atlantic Ocean and North Pacific relatively well, but scarcely covered the Indian Ocean and South Pacific.

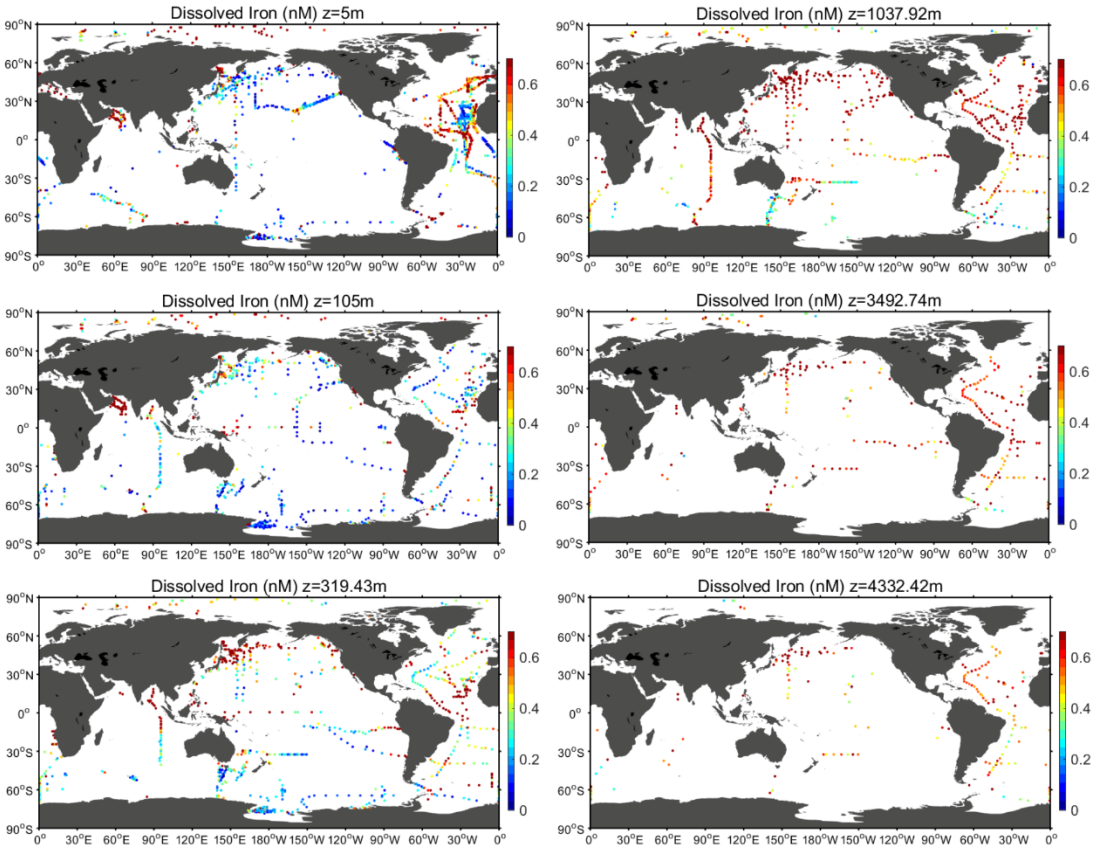

Figure 3. Horizontal map of *dFe* observational data (nmol L^{-1}), which was constructed by merging the three observational databases, GEOTRACES IDP2017, the historical data compiled by Moore and Braucher (2008) and Tagliabue et al. (2012), and the North Pacific Ocean data by Yamashita et al. (2020) and Nishioka et al. (2020). The merged data were considered as climatological data.

2.3 Dynamical interpolation

We carried out a data synthesis in which information available from observations was integrated to obtain a set of optimized model parameters. A Green's function approach is known to be a powerful tool for data synthesis. Menemenlis et al. (2005) have successfully applied a Green's function approach to an OGCM, and Toyoda et al. (2013) and more recently Brix et al. (2015) and Doi et al. (2015) have used this method with a biogeochemical model. In this study, we used a Green's function approach because of its simplicity and power.

We searched for an optimal set of model parameter values for the iron cycle model by minimizing the following cost function:

$$\mathrm{J}(\boldsymbol{x}) = \frac{1}{2}[\mathrm{H}(\boldsymbol{x}) - \boldsymbol{y}]^T \mathbf{R}^{-1}[\mathrm{H}(\boldsymbol{x}) - \boldsymbol{y}] \tag{9}$$

where $\boldsymbol{x}$ is the control variable, $\boldsymbol{y}$ is an observation, $\mathbf{R}$ is the observation error covariance matrix, and H is the observation operator including the model time integration. If a linear approximation is used for the observation operator, equation (9) has the following stationary solution:

$$\hat{\boldsymbol{x}} = \boldsymbol{x}_b - (\mathbf{DH}^T \mathrm{R}^{-1}\mathbf{DH})^{-1} \times \{\mathbf{DH}^T \mathrm{R}^{-1}[H(\boldsymbol{x}_b) - \boldsymbol{y}]\} \tag{10}$$

where $\boldsymbol{x}_b$ is the first guess. The derivative **DH** is approximated by a Green's function (Menemenlis et al., 2005):

$$(\mathbf{DH})_{\boldsymbol{j}} \cong \frac{\mathrm{H}(\boldsymbol{x}_b + \boldsymbol{e}_j) - \mathrm{H}(\boldsymbol{x}_b)}{\|\boldsymbol{e}_j\|} \tag{11}$$

where $\boldsymbol{e}_j$ is the perturbation of the *j*-th parameter. The optimal solution $\hat{\boldsymbol{x}}$ is thus computed from the results of perturbed model integrations $\mathrm{H}(\boldsymbol{x}_b + \boldsymbol{e}_j)$. The component of the cost terms with our Green's function approach incorporates observations. As observational data, we used the merged *dFe* concentration data (section 2.2).

For the optimization, we used ten parameters as control variables: desorption or dissolution rate; scavenging rate; sinking velocity; ligand concentration; proportionality coefficient; consumption rate by phytoplankton; and supply rate from the seafloor. Desorption or dissolution rate, scavenging rate, and sinking velocity were assigned to dust and POC, respectively. These control variables correspond to the processes shown in Figure 1. Since the characteristics of the ocean general circulation and material cycle vary depending on the basin, it is considered that the iron cycle also has differences among basins. So, we divided the global ocean into five basins, as shown in Figure 4, and the ten parameters were optimized to fit the observational data in each of the five basins.

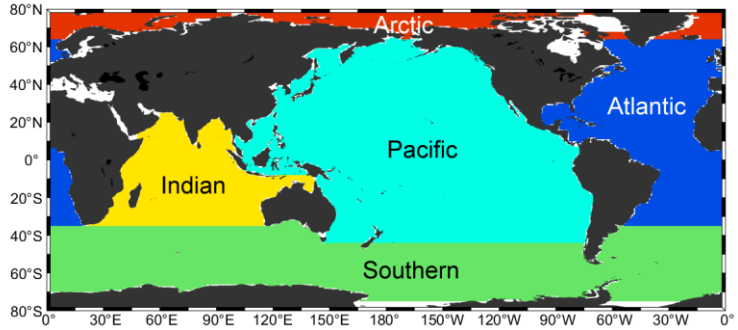

Figure 4. Delineation of each basin used in this study. The northern boundary was set at 64˚N. The southern boundary was set at 35˚S in the Atlantic Ocean and Indian Ocean and at 44˚S in Pacific Ocean.

First, we searched out a set of ten parameters that could reproduce the averaged observational *dFe* concentration in the global ocean. Values of the ligand concentration and proportionality coefficient were chosen based on Moore and Braucher (2008); other parameter values were set arbitrarily. The set of ten parameter values shown in Table 1 were applied to all basins as the first guess $\boldsymbol{x}_b$. As the control run, we carried out an iron cycle model simulation by using this parameter set $\boldsymbol{x}_b$ until the annual mean iron concentration was in steady state. Next, we carried out the ten perturbation experiments by perturbing the ten control variables with the perturbation parameters $\boldsymbol{e}_j$ in each basin. Although the optimal solution was obtained with equation (10) by using the results of the control model and the perturbed models, we iterated equations (10) and (11) to obtain the stationary value of the cost function J($\boldsymbol{x}$). During the iteration, perturbation parameters $\boldsymbol{e}_j$ were applied with a common value in each basin. We completed the iteration when the value of the cost function changed by ≤ 1%. Finally, we obtained that solution $\hat{\boldsymbol{x}}$ as the optimal solution.

3. Validation of estimations

3.1 Optimized parameters

Table 1 shows the optimized values of the control variables for each basin along with the values for the first guess. The reduction rate of the cost is based on a comparison of the costs in the control run versus the optimized run, which were estimated with equation (9). A positive value means that the cost was smaller for the optimized run than for the control run. Optimization reduced the cost in every basin.

The estimated dissolution rate from POC was higher than that from aeolian dust in all basins. The dissolution rates from POC were similar in every basin. However, the dissolution rate from aeolian dust was low in the Pacific Ocean and Southern Ocean, and high in the Atlantic

Ocean, Indian Ocean and Arctic Ocean. The rate of adsorption to particles was prescribed by the scavenging rate. In all basins, the scavenging rate by POC was higher than the rate by aeolian dust. In the Indian Ocean and Southern Ocean, the scavenging rate by POC was about 4.5 times the rate by aeolian dust, and in the Pacific Ocean and Arctic Ocean, the scavenging rate by POC was about twice the rate by aeolian dust. In the Atlantic Ocean, the difference in scavenging rate was largest, and the rate by aeolian dust was less than one tenth the rate by POC. The sinking velocity of POC particles were the slowest in the Atlantic Ocean and the fastest in the Arctic Ocean. The range of the sinking velocity of POC particles was not large, 2.1–3.3 m day^{-1}. On the other hand, the sinking velocity of aeolian dust particles differed greatly among basins, from ~1.8 m day^{-1} in the Indian Ocean to ~10.2 m day^{-1} in the Pacific Ocean. Only in the Indian Ocean, the sinking velocity of POC was faster than the aeolian dust, and in other basins, the sinking velocity of aeolian dust was faster. Especially, the sinking velocity of aeolian dust in the Pacific Ocean was estimated to be large. As shown in equation (4), this model increases the rate of *dFe* adsorption when the concentration of *dFe* exceeds the ligand concentration. The proportionality coefficient prescribes how much adsorption is increased. The ligand concentrations in all basins were estimated to lie in the range 0.29–0.41 nmol L^{-1}; these values are estimated below the commonly used value of 0.6 nmol L^{-1} (Moore & Braucher, 2008). The highest ligand concentration, ~0.41 nmol L^{-1}, and the smallest proportionality coefficient, ~0.0014, were estimated in the Pacific Ocean. The combination of the highest ligand concentration and the smallest proportionality coefficient suggests that scavenging by particles occurs more slowly in the Pacific Ocean than in other basins. The implication is that the *dFe* stays in the water column for a longer time in the Pacific Ocean. The supply rate from shelf sediment was highest in the Atlantic Ocean, next highest in the Pacific Ocean, and lowest in the Southern Ocean. It was estimated that large amounts of iron should be supplied from sediments in the Atlantic and Pacific Oceans. The consumption rate by phytoplankton in the Southern Ocean was small compared with that in other basins. Because the model was run offline, the consumption of *dFe* was estimated using the given phytoplankton distribution. The Fe/C ratio of phytoplankton uptake varies depending on the phytoplankton species and environmental conditions. The estimated result of the consumption rate by the model represented by one phytoplankton is a value assuming a virtual species of phytoplankton which averaged many conditions. If species of phytoplankton were considered, the analysis had been conducted online, or observations were increased spatiotemporally, the optimized consumption rates would have been estimated somewhat differently.

The optimized parameter set for the five basins revealed the differences in the dynamics of the iron cycle in each basin. In the following section, we discuss the results of the estimation executed using the optimized parameters for each basin, with the exception of the Arctic Ocean. Since the treatment of the Arctic Ocean in the physical model was auxiliary and there

were very few iron observational data, the results of the Arctic Ocean were not mentioned.

Table 1

Optimized values for the control variables estimated by the Green's function approach

Parameter	First guess	Optimized values					
		Atlantic	Pacific	Southern	Indian	Arctic	Global
Desorption or Dissolution Rate from POC (% day^{-1})	1.302	1.330	1.308	1.308	1.306	1.301	
Desorption or Dissolution Rate from Aeolian Dust (% day^{-1})	0.127	0.117	0.062	0.074	0.141	0.124	
Sinking Velocity of POC (m day^{-1})	3.291	2.149	3.102	3.016	3.153	3.325	
Sinking Velocity of Dust (m day^{-1})	3.291	3.551	10.196	4.751	1.822	3.747	
Scavenging Rate by POC (L gC^{-1} day^{-1})	68.31	95.87	87.56	91.43	88.62	68.69	
Scavenging Rate by Dust (L g^{-1} day^{-1})	33.76	6.60	43.68	20.41	20.00	34.29	
Ligand Concentration (nmol L^{-1})	0.392	0.341	0.412	0.285	0.374	0.386	
Proportional Coefficient (L μmol^{-1} day^{-1})	8.94	16.12	1.38	4.72	7.14	10.91	
Consumption Rate by Phytoplankton (nmol $mgChl^{-1}$ day^{-1})	1.939	1.671	2.365	1.181	2.058	1.943	
Supply Rate from Seafloor (nmol m^{-2} day^{-1})	848.3	1827.8	1125.9	485.9	732.4	594.4	
Percentage Reduction of Cost		16.9%	23.6%	20.7%	29.5%	31.3%	20.7%

3.2 Cost reductions

We ran the iron cycle model with the parameter set that was optimized for the five basins by the Green's function approach. Steady state in the annual cycle of the model was obtained after an integration over time of 150 years. The fluctuation of the annual mean total amount of *dFe* was estimated to be 0.00001% $year^{-1}$.

Table 1 shows the results of the cost comparisons. The costs decreased by 16.9%, 23.6%, 20.7%, 29.5%, and 31.3% in the Atlantic, Pacific, Southern, Indian, and Arctic oceans, respectively. The average reduction rate for the global ocean was 20.7%. To visualize the

effect of the cost reduction, we compared the estimated and observed *dFe* concentrations (Figure 5). The orange and black dots are the results for the control run and optimized run, respectively. The improvement in the correspondence for the optimized run was apparent in every basin; the black dots lie much closer to the 1:1 line. The correlation coefficients between observed and estimated *dFe* concentrations increased from the first guess to the optimized result. The correlation coefficients between the model results and observations at corresponding locations were all significant at the 95% confidence level. The correlation coefficients for the first guess in the Atlantic, Pacific, Southern, and Indian Oceans were 0.11, 0.24, 0.16, and 0.72, respectively. The correlation coefficients for the optimized results improved to 0.17, 0.29, 0.18, and 0.74, respectively. In the Arctic Ocean, the correlation coefficients were negative and ranged from −0.12 of the first guess to −0.23 of the optimized result. The number of observational data used was 98, which was very few, and the relationships seemed to differ among the Arctic Ocean and other basins.

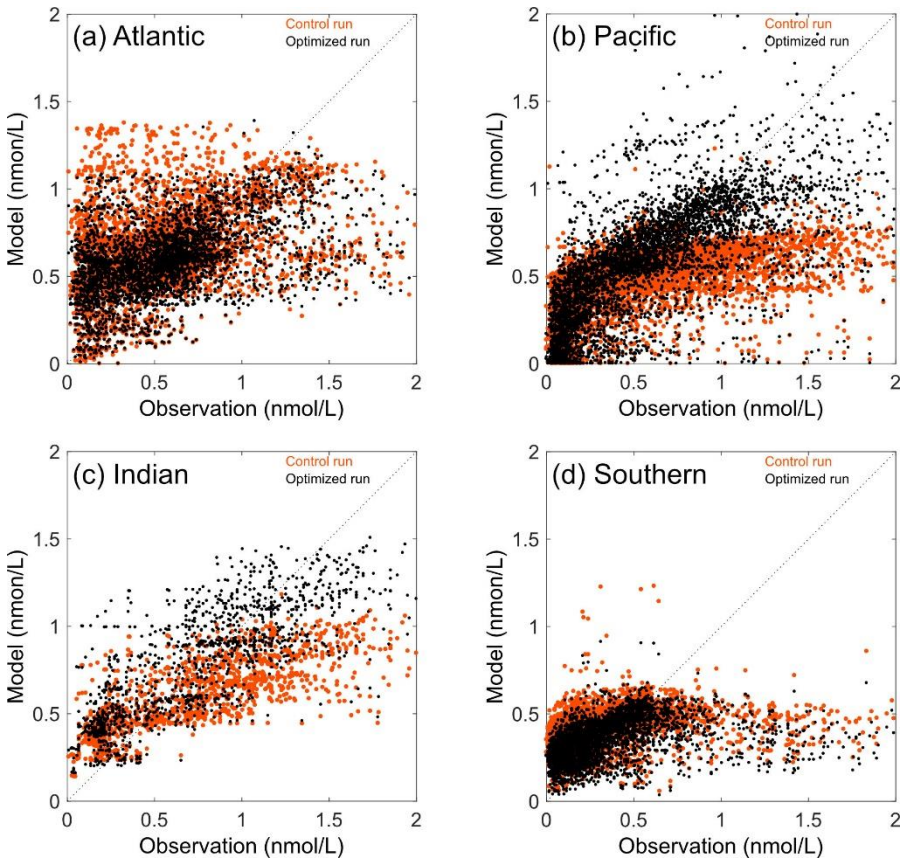

Figure 5. Scatter diagrams between the estimated and observed *dFe* concentrations in the (a) Atlantic Ocean, (b) Pacific Ocean, (c) Indian Ocean, and (d) Southern Ocean. The black and orange dots indicate the results of the optimized and control runs, respectively. Comparisons were made at grid points where there were observational data. The dotted lines are the 1:1 line.

4. Estimation of the global oceanic iron distribution

4.1 Description of the climatology

Figure 6 shows the horizontal distribution of the annual mean *dFe* concentrations obtained with the optimized run. The observed concentrations are also plotted as solid circles on the map using the same color scale. The horizontal distribution of the estimated results at each depth layers were in broad agreement with the distribution of aeolian dust shown in Figure 2. There were regions of high *dFe* concentrations at low latitudes in the Atlantic Ocean. In the Pacific Ocean, regions of high *dFe* concentration were apparent in the western North Pacific, and the eastern Pacific at low latitudes. Moreover, a region of high *dFe* concentrations was also apparent in the western Pacific Ocean, in the region from Maritime Continent to Australia, and in the northern Indian Ocean. A common feature of the *dFe* distributions in these regions was that the *dFe* concentrations were high from the sea surface to the seafloor. Because the distribution of *dFe* concentrations resembled the distribution of aeolian dust, we hypothesized that the dissolution of iron from aeolian dust sinking through the water column accounted for this pattern. However, as shown in Table 1, the optimized parameters in each basin suggested that the processes involved in the iron cycle differed in each basin. In particular, sinking velocity and scavenging rate of the aeolian dust were very different between the Atlantic and Pacific Oceans. These differences are discussed in section 4.4.

In the upper layer, from the surface to a depth of 200 m (epipelagic zone), the comparison reveals that the estimated and observed concentrations at many locations did not coincide. Variations in meteorological conditions such as rainfall or seasonal variations of the mixed layer depth can have a large effect on observed *dFe* concentrations. Considering that the observations were sparsely distributed spatially and temporally, discussing the representativeness of the observed concentrations in the epipelagic zone is problematic, and it is also problematic to compare those *dFe* concentrations with the results of the climatological model. On the other hand, at depths greater than 300 m, where the influence of meteorological conditions and seasonal variations becomes small, the horizontal distribution of the estimated high and low *dFe* concentrations on a basin scale were by and large reproduced the observed distribution. By using only the observations ranging from the depth of 300 m to the bottom and excluding the high concentration value on the ocean ridge which seems to be the influence of the hydrothermal plume, we re-estimated the correlation coefficient. That shown in Section 3.2 was the values estimated by using all observations. The result in the Atlantic, Pacific, Southern, and Indian Oceans were 0.55, 0.61, 0.41, and 0.75, respectively. The root mean square error (RMSE) estimated by the same data were 0.27, 0.38, 0.21, and 0.23 nmol L^{-1}, respectively. Since the REMS estimated from the result of control run were 0.28, 0.50, 0.23, and 0.30 nmol L^{-1}, respectively, the effect of the optimization by data synthesis approach was shown. In the mesopelagic zone northeast of

New Zealand and in the Southern Ocean, the estimated *dFe* concentrations did not decrease in the same range as the observed concentrations. The estimated result of our current model seems that has tend not to decrease as low as the observations in the region of low concentrations. The observed high concentrations that appeared on the ridge at a depth of ~3000 m was not reproduced by our model because the iron supply from hydrothermal plumes on the seafloor was not taken into account in our model.

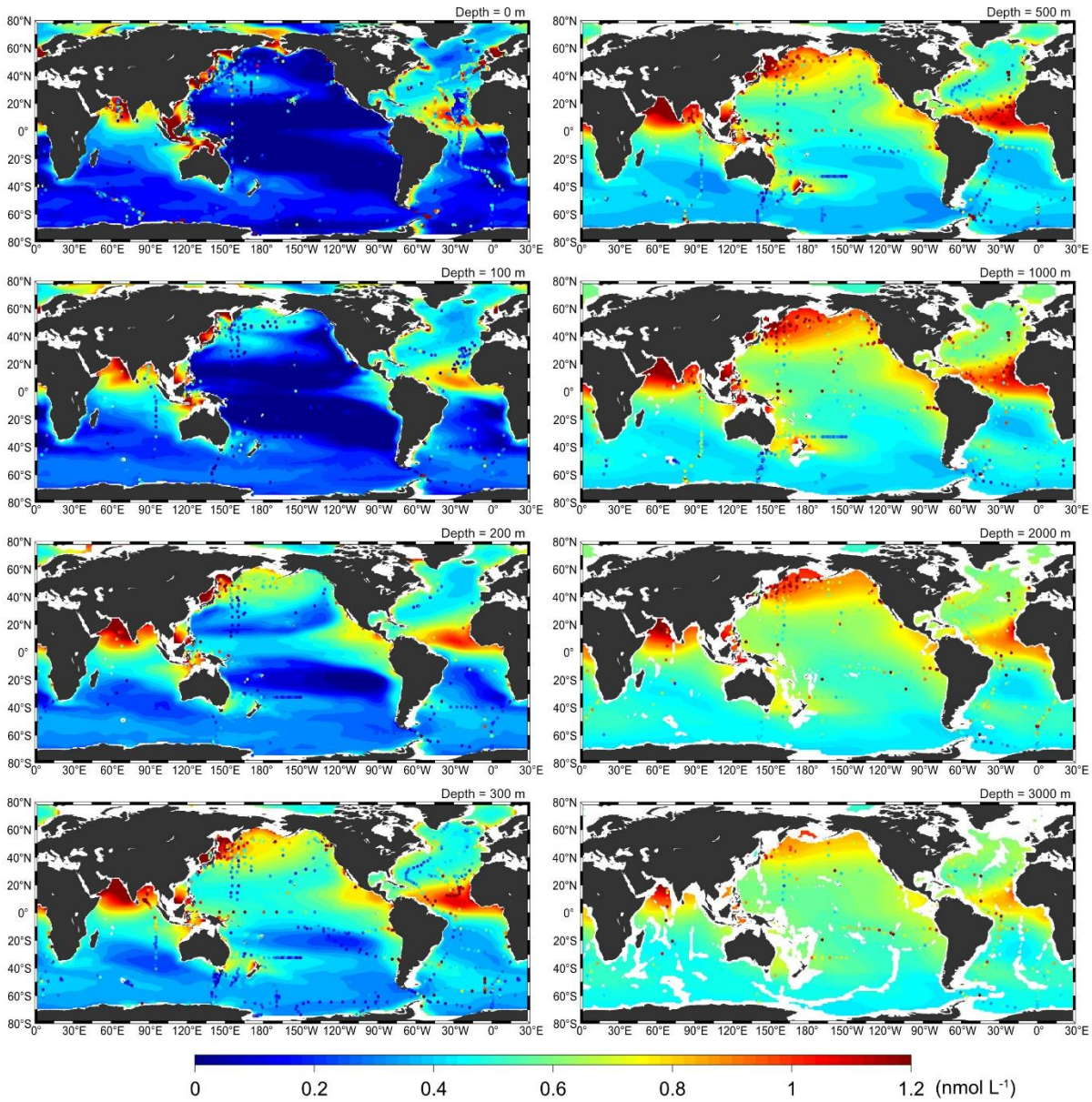

Figure 6. Horizontal distribution of the *dFe* concentration at representative depths. The units are nmol L^{-1}. The observations are shown by solid circles over the estimated results and use the same color scale as the latter.

Figure 7 compares our estimates with some vertical sections of the GEOTRACES program. Figures 7a, 7b, and 7c show zonal sections in the Atlantic Ocean. Estimated *dFe* concentrations along the observational sections at GA03w (Figure 7a upper) and GAc01 (Figure 7b upper) were compared with those observed in GA03w (Figure 7a lower, Fitzsimmons et al., 2015; Hatta et al., 2014) and GAc01 (Figure 7b lower, Saito et al., 2013). The waters containing high observed concentrations were apparent in eastern and western offshore regions, and over the mid-ocean ridge. The estimated concentrations in Figure 7a shows that the high *dFe* distributions in eastern and western offshores are well reproduced. The *dFe* concentration was low in the epipelagic zone, but did not reach low as much as observed. The estimated concentrations in Figure 7b shows the high *dFe* distributions in eastern and western offshores as with the observation, but the estimated concentration was lower than observation. In the western part of observed section, waters with a high *dFe* concentration were apparent at a depth of ~3000 m. The region of high *dFe* concentration in the estimated result was further west of the observation, but at similar depths. This high *dFe* concentration in the western deep appears to be formed by the transport of high *dFe* concentrations from the equatorial region by the southward flow of North Atlantic deep water. High concentrations over the mid-ocean ridge were observed both the observational sections at GA03w and GAc01. Because these patterns are likely the result of hydrothermal venting, the optimized model did not simulate this extend of high concentrations. In the 40˚S zonal section (Figure 7c lower, GA10), the tendency of high *dFe* concentrations near eastern and western continental shelf were estimated, but supply of iron on the African coast seems underestimated. Low concentrations in the epipelagic zone tended to extend into the mesopelagic zone around eastern region, which was consistent with the observation. High concentration water on the east side of the top of the mid-ocean ridge, which was not shown in the estimated result, was likely to be iron from hydrothermal supply. In Antarctic Bottom Water (AABW), which fills the bottom layer between the mid-ocean ridge and the African continent, decreasing *dFe* concentration near the seafloor was observed, but the corresponding distribution of low *dFe* concentration did not appear in the estimated result. It seems that the difference in concentration did not appear because the estimated *dFe* concentration in the bottom layer surrounding this zonal section was about 0.5 nmol L^{-1} everywhere. Figure 7d shows a meridional section of the Atlantic Ocean (GA02: Rijkenberg et al., 2014). The estimated and observed concentrations were high near 35˚S, 10˚N, and 45˚N that the meridional distributions were in good agreement. The observed high concentrations at depths of 2000–3000 m in the equatorial region and in 35˚S are likely the iron supplied from hydrothermal on the seafloor. There were discrepancies in the vertical distributions of estimated and observed high *dFe* concentrations. The estimated concentrations tended to stretch vertically. The distribution of observed concentrations suggests that the *dFe* concentration tends to be low in the bathypelagic zone. The vertical

transport of iron by settling particles in the Atlantic Ocean may have been somewhat overestimated in our estimation.

In the zonal section of the North Pacific Ocean (Figure 7e), the optimized result successfully reproduced the distribution which was reported in observational study (GP02: Nishioka & Obata, 2017); the input of iron from the Sea of Okhotsk through the Kuril Strait and its advection to the east and into the mesopelagic zone. The result also reproduced a distribution of *dFe* that suggested a supply from the shelf sediments in the eastern Pacific basin. We examined a combination of some trial parameters before obtaining this optimized result. In the case of the tuned parameters based on Moore and Braucher (2008) settings, we obtained a distribution of *dFe* concentrations that did not much change from the surface to the ocean bottom. That is, the horizontal distribution of *dFe* concentration at any depth was similar to the distribution of dust deposition shown in Figure 2. We also examined the distribution of *dFe* when the vertical transport of iron by particles were constrained, which was realized by set a slow settling velocity of particles and a large ligand concentration. As the result, *dFe* concentration became high in the bathypelagic zone throughout the South Pacific Ocean. The characteristics of the optimal parameters in the Pacific Ocean revealed from these analyses was that the proportionality coefficient C_{high} was much smaller than the value based on Moore and Braucher (2008), the sinking velocity of dust particles was fast, and the supply rate of the iron from the shelf sediments was high. The estimated result using optimized parameters successfully reproduced the situation in which iron supplied from shelf sediment was diffused slowly in the vertical direction while transported to the horizontal direction in the intercontinental scale. In the 10˚S zonal section (Figure 7f) of the estimated result, *dFe* was supplied from shelf sediments near the Solomon Islands and near the coast of Peru, and *dFe* concentration in the epipelagic zone was very low. The correspondence between the region of high estimated *dFe* concentrations in the eastern basin and the observed distribution (GP16: John et al., 2018; Sanial et al., 2018) suggests that *dFe* is supplied from the coast of Peru. However, the estimated concentration only supplying from the shelf sediments was low compared with the observation, and it should be necessary to consider the complicated supply process due to the resuspension from a wide region of the continental slope (John et al., 2018). A supply of *dFe* from the East Pacific Rise (Fitzsimmons et al., 2017; Resing et al., 2015) was not included in this estimation due to the hydrothermal supply. In the 30˚S section (Figure 7g), there was a region of high estimated *dFe* concentrations around the western shelf that was similar to the observed distribution near the western region of this section (GP13: Ellwood et al., 2018). Because the observed distribution suggests the existence of a source in the deeper layer at around 160˚E or 180˚ longitude, it seems likely that there is a supply of *dFe* from hydrothermal plumes that should not be neglected in this region. Figure 7h shows the distribution of estimated *dFe* and observed *dFe* (Yamashita et al., 2020) on the 155˚E meridional section. The estimated distribution indicated that *dFe* supplied from the Sea of

Okhotsk was transported toward the south, and hence the *dFe* concentration reached low around 20˚N. This distribution corresponds to the observation well.

The last comparison of estimated and observed *dFe* concentrations was along the 70˚E meridional section in the Indian Ocean (Figure 7i). The observations showed that the northern Arabian Sea is a region of high *dFe* concentrations. The estimated region of the northern high *dFe* concentrations were consistent with the observations, although the estimated concentrations were somewhat higher. The observed distribution that stretch south–north around the seafloor of the Indian Ocean also suggests a large supply of iron from hydrothermal plumes (Nishioka et al., 2013; Vu & Sohrin, 2013). Because there were few observations in the Indian Ocean, it seems that the influence of high concentrations around the seafloor on the optimization was relatively strong. As the results, the high dissolution rate and slow sinking velocity of the aeolian dust were estimated by the optimization (Table 1). These parameter sets further increased the dissolution of iron from aeolian dust into the water column.

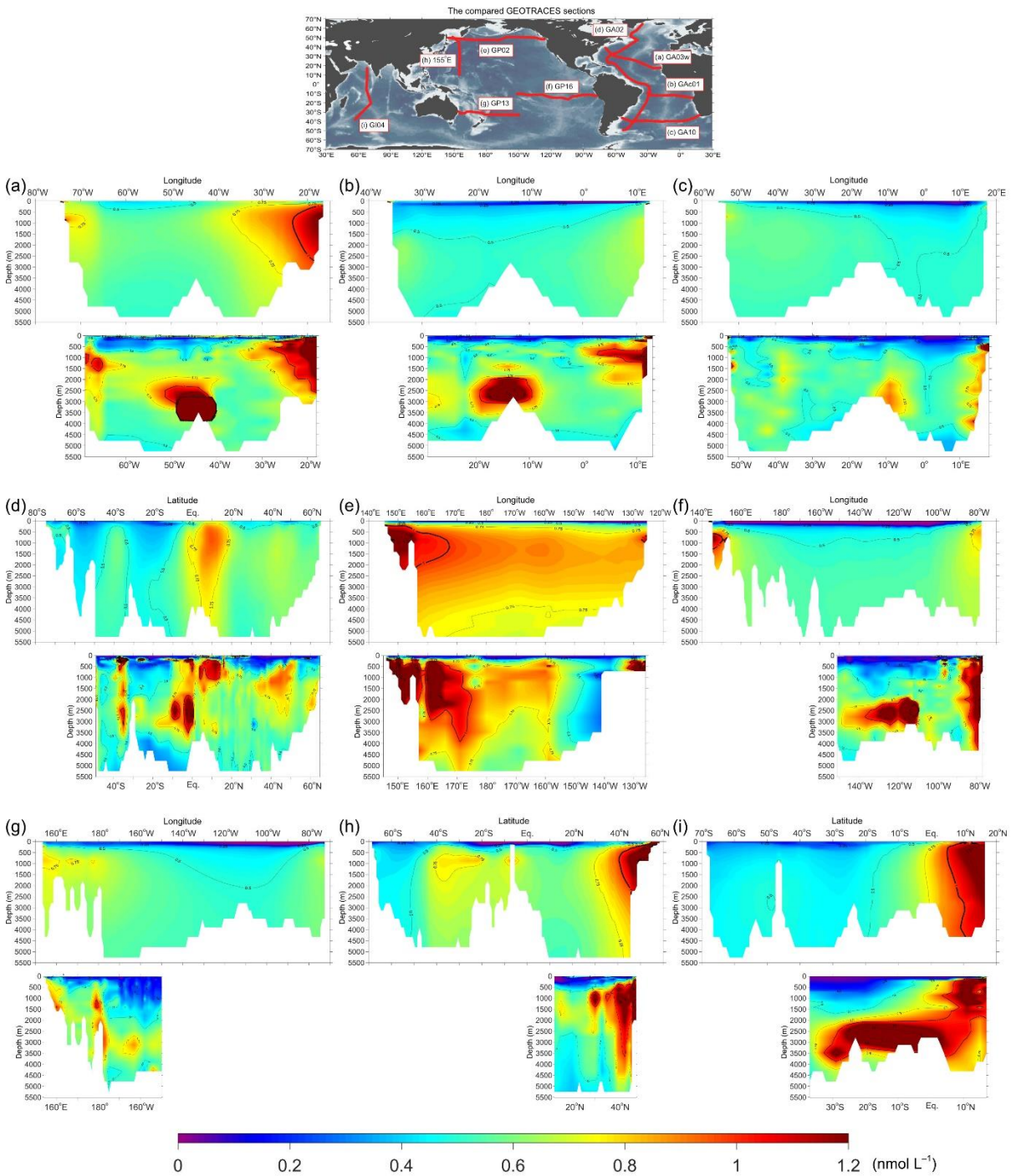

Figure 7. Vertical section plots of *dFe* distributions. The units are nmol L^{-1}. Panels (a), (b), and (c) are zonal sections, and (d) is a meridional section in the Atlantic Ocean. Panels (e), (f), and (g) are zonal sections, and (h) is a meridional section in the Pacific Ocean. Panel (i) is a meridional section in the Indian Ocean. Each panel displays the distribution of estimated (upper) and observed (lower) *dFe* concentrations.

4.2 Seasonal variations

Figure 9 shows the annual fluctuations of the layer-averaged *dFe* concentrations. The values

were equated to the differences between the maximum and minimum concentrations over an annual cycle in each layer. Because the model assumed a constant supply of iron from the sediment, the seasonal variations of the *dFe* concentrations were controlled by monthly aeolian dust fluxes, the distribution of monthly mean phytoplankton and POC biomass, and the annual cycle of ocean physics. The largest fluctuations occurred at the surface of the Indian Ocean, 0.07 nmol L^{-1}. The smallest fluctuations at the surface were found in the Pacific Ocean, 0.015 nmol L^{-1}. At a depth of ~100 m in each basin, there was an inflection point of the rate of fluctuation attenuation, and the fluctuations decreased toward a depth of 800 m from there. There was little evidence of seasonal variations below a depth of 1000 m, with the exception of the Indian Ocean. Below a depth of 900 m in the Indian Ocean, the seasonal variations of ~0.005 nmol L^{-1} suggest that the response to the physical field is barotropic. Future work will explore the possibility of seasonal variations in the supply of iron from sediments. It is a challenge to obtain the seasonal observational data in order to understand the seasonal variation characteristics of *dFe* and therefore validate the model study.

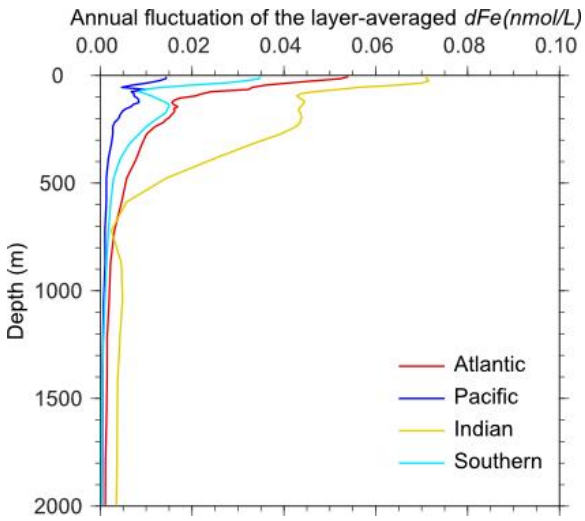

Figure 8. Annual fluctuations of layer-averaged *dFe* concentrations.

4.3 Iron cycle

We used the *dFe* concentrations obtained from the optimized model to investigate how *dFe* moves through the ocean via the flow field and exchanges with particle matter. Figure 10 shows the calculated fluxes for each process, and Table 2 provides a summary of the *dFe* concentrations in each basin. MERRA-2 monthly mean dust data were used as the aeolian dust data. If we assume that the iron content of the dust was 3.5% (section 2), the input of iron from aeolian dust to the global ocean was 120.2 Gmol yr^{-1} (Figure 10a). In accord with Moore and Braucher (2008), we assumed that 2.0% of the aeolian iron dissolved instantaneously at the sea surface. This instantaneous input of *dFe* from aeolian iron to the

surface water amounted to 2.4 Gmol yr^{-1}. Of the remaining aeolian iron, 10.4 Gmol yr^{-1} dissolved into the ocean during the sinking of dust particles. A total of 12.8 Gmol yr^{-1} of iron derived from aeolian dust therefore dissolved into the ocean. The remaining 107.4 Gmol yr^{-1} sank along with dust particles and arrived at the seafloor. The sum of the estimated inputs of *dFe* from the sediments (11.8 Gmol yr^{-1}) and aeolian iron (12.8 Gmol yr^{-1}) was therefore 24.6 Gmol yr^{-1}. The consumption by phytoplankton was estimated to be 6.3 Gmol yr^{-1}, and an estimated 25.0 Gmol yr^{-1} was captured by suspended organic particles and removed from the water column. Our estimates thus depict an iron cycle in which *dFe* enters the ocean from the atmosphere or from shelf sediment and is removed at the seafloor through sinking of particulate organic matter. The estimated standing stock of *dFe* in the global ocean was 748 Gmol, the average concentration was 0.58 nmol L^{-1}, and the residence time averaged throughout the global ocean was 30.4 years (Table 2). These estimates are within the range of results from other iron cycle models summarized by Tagliabue et al. (2016). In particular, our estimates are near the corresponding values from the PICES model (Aumont et al., 2015; Resing et al., 2015).

The *dFe* concentrations and residence times estimated with our model for every basin revealed characteristic differences between basins. The estimated input of iron from aeolian dust to the Atlantic Ocean was 67.2 Gmol yr^{-1} (Figure 10b) but only 23.1 Gmol yr^{-1} to the Pacific Ocean, about one-third the input to the Atlantic Ocean (Figure 10c). Dissolution from shelf sediment was similar in the two basins: 4.4 Gmol yr^{-1} in the Atlantic and 4.1 Gmol yr^{-1} in the Pacific. The estimated net dissolution rate of aeolian iron into the ocean was 7.6 Gmol yr^{-1} in the Atlantic and 0.4 Gmol yr^{-1} in the Pacific. The input of *dFe* via dissolution of aeolian iron in the Pacific was very small compared with the Atlantic. The amount of iron removed to the sediments by sinking organic particles was 11.9 Gmol yr^{-1} in the Atlantic and 4.1 Gmol yr^{-1} in the Pacific. The residence time of *dFe* was estimated to be 12.2 years in the Atlantic and 80.4 years in the Pacific. The averaged *dFe* concentrations were estimated to be 0.62 nmol L^{-1} in the Atlantic and 0.61 nmol L^{-1} in the Pacific. In the Atlantic Ocean, the flux of iron dissolution and scavenging through particles were very large compared with the Pacific Ocean, and the residence time of *dFe* was short. This suggests that the aeolian iron plays a dominant role in the formation of *dFe* distribution in many regions of the Atlantic Ocean. The high *dFe* concentration around 10˚N in the meridional section (Figure 7d) corresponds to the location of the atmosphere containing a large amount of dust particles in the Atlantic Ocean (Figure 2). Figure 7d also shows the vertically spread distribution of *dFe* concentration, and it can be seen that the influence of vertical transport due to sinking particles is large. Whereas the Pacific Ocean, since the net supply from aeolian iron is small, the ratio of iron supplied from sediments is relatively high. Because of the very long residence time, it is considered that the distribution of *dFe* in the mesopelagic and bathypelagic regions in the Pacific Ocean are formed under the influence of advection and

diffusion over a long time.

In the Indian Ocean, the input of *dFe* via dissolution from aeolian iron (3.0 Gmol yr^{-1}) was estimated to be about three times the rate via dissolution of sediments (1.1 Gmol yr^{-1}) (Figure 10d and Table 2). It seems that there is a large input of aeolian iron to the Arabian Sea. The residence time and the average concentration of *dFe* in the Indian Ocean were estimated to be 23.7 years and 0.62 nmol L^{-1}, respectively. The estimated inputs of *dFe* via dissolution of aeolian iron and sediments in the Southern Ocean were 1.7 Gmol yr^{-1} and 0.8 Gmol yr^{-1}, respectively (Figure 10e). The residence time of *dFe* was estimated to be 57.2 years. The Southern Ocean was the basin that the *dFe* remains in the water column for the second longest time. The estimated average concentration, 0.46 nmol L^{-1}, was the lowest among all basins.

The fluxes of *dFe* between basins by advection and diffusion were relatively small. Figure 10 also shows the flux of inflow and outflow to each basin. It was shown that *dFe* was transported toward high-latitude regions from low-latitude by advection and diffusion.

In this model, the iron cycle was represented by the flux of iron that enters from the aeolian dust or shelf sediments and reaches the seafloor through biogeochemical processes. Since hydrothermal plumes play an important role in forming the distribution of dissolved matter in the mesopelagic and bathypelagic regions (e.g., Frants et al., 2016; Resing et al., 2015), iron source from hydrothermal also should be added to current sources in future work. Including iron supplies from hydrothermal in our optimization would change the current estimation; the amount of iron supply from shelf sediments may somewhat reduce; iron flux due to interaction through particles may change; the average concentration of the basin may increase a little; the ligand concentration also could be change. Assuming the supply rate of iron from hydrothermal in the global ocean ~0.7 Gmol yr^{-1} (Bennett et al., 2008, Frants et al., 2016), it corresponds to 2.4% of the total supply in our current estimation. Therefore, including hydrothermal supply in our optimization should improve the reproducibility of *dFe* distribution in the mesopelagic and bathypelagic regions, however, the features of the basin's iron cycle evaluated in our optimization may not be sensitive to considering hydrothermal supply.

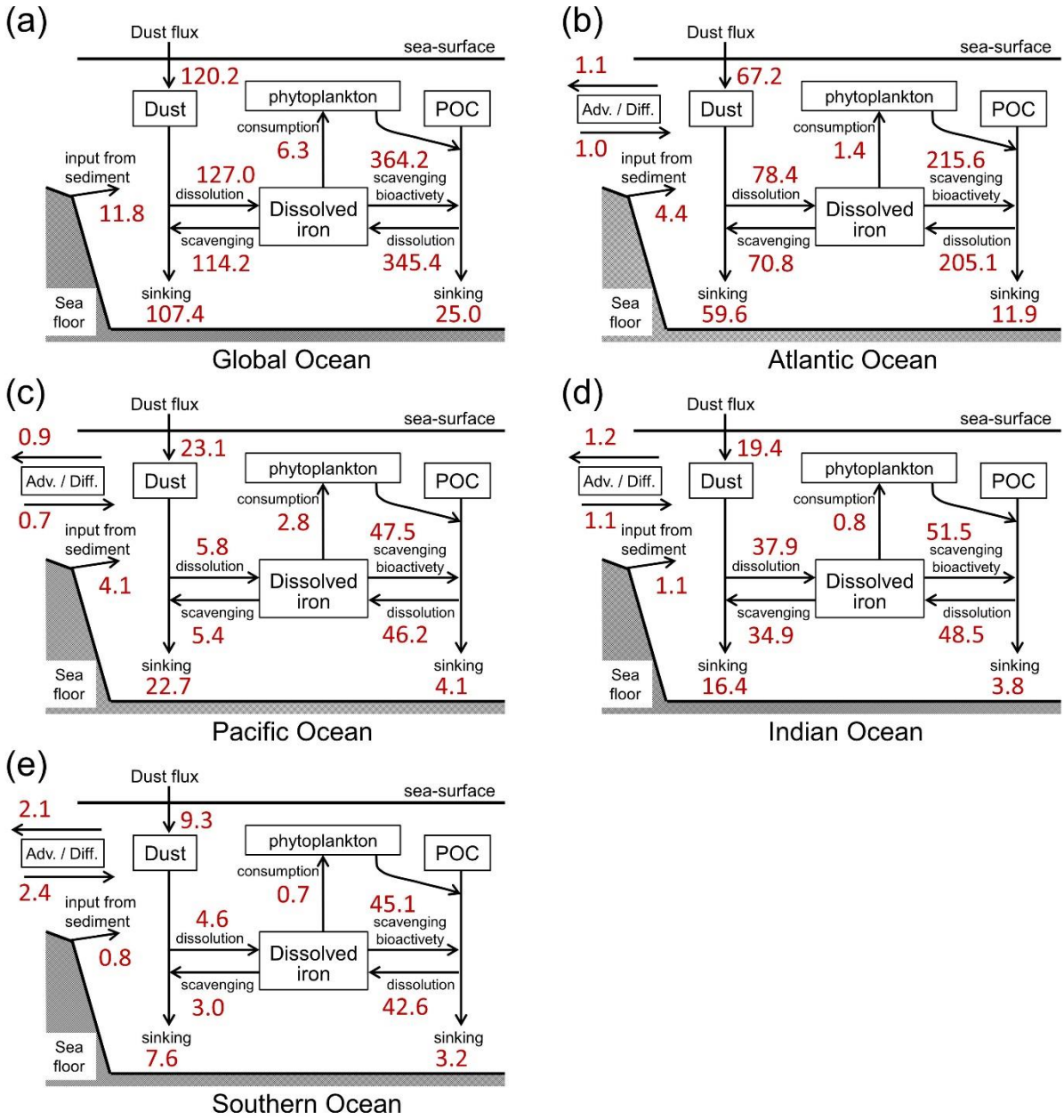

Figure 9. Annual budgets of *dFe* obtained from the optimized model for (a) the global ocean and the (b) Atlantic, (c) Pacific, (d) Indian, and (e) Southern. The units are Gmol yr^{-1}.

Table 2

Summary of dFe metrics in the ocean basins

	Fe source (Gmol year^{-1})			Fe inventory (Gmol)	Average Fe (nmol L^{-1})	Residence time (year)
	Dust	Sediment	Total			
Global Ocean	12.8	11.8	24.6	748	0.58	30.4
Atlantic Ocean	7.6	4.4	12.0	146	0.62	12.2
Pacific Ocean	0.4	4.1	4.5	360	0.61	80.4
Indian Ocean	3.0	1.1	4.1	98	0.62	23.7
Southern Ocean	1.7	0.8	2.5	141	0.46	57.2

5. Conclusions

By using both a model and available observations, we constructed a gridded three-dimensional *dFe* dataset for the global ocean. Although the ocean iron cycle model was simple, it simulated the seasonal *dFe* distribution throughout the water column, and where there was sparse observational data, the model interpolated spatiotemporally with a dynamical consistency. A set of optimized parameters for expressing iron cycle processes was defined for each basin based on the observed data. By assimilating the observational data, the average concentration and distribution were reproduced, except for the distribution due to the influence of hydrothermal plumes. The optimized results successfully captured the features of the iron cycle in each basin. For example, the *dFe* distribution in the Atlantic Ocean was strongly affected by aeolian iron, whereas in the Pacific Ocean, the iron supply from shelf sediments had a greater impact on the iron distribution.

In the model, the supply of *dFe* from hydrothermal plumes on ridges was not considered, and the inputs from shelf sediments were spatiotemporally invariant. Moreover, the transport of *dFe* was calculated using an offline model to which the physical field was provided as input. In a future study, the regional influence of iron supply from shelf sediments and the effects of hydrothermal plumes will be investigated, and the iron cycle model will be integrated into an online model in order to update the three-dimensional gridded dataset of *dFe* concentration. The improved model is expected to be useful for predicting and analyzing the effects of spatiotemporal variations of *dFe* on primary production and the associated response of a lower-trophic-level ecosystem.

The basin-scale model of the *dFe* cycle used in this study is a simplified characterization that bundles many physical and chemical elementary processes. We expect that a simplified analysis of these complex processes will provide important implications for leading to more realistic and detailed understanding of the biogeochemical processes.

Acknowledgments and Data Availability

This work was supported in part by a Grant-in-Aid for Scientific Research on Innovative Areas (MEXT KAKENHI-JP15H05817/JP15H05819). The numerical calculations were carried out on the Earth Simulator and the DA System supported by the Japan Agency for Marine-Earth Science and Technology (JAMSTEC). The ESTOC ocean state estimate dataset, doi:10.17596/0000106, has been published on the JAMSTEC web site (http://www.godac.jamstec.go.jp/estoc/e/top/).
The SeaWiFS products are distributed online (https://oceandata.sci.gsfc.nasa.gov/SeaWiFS/Mapped/Monthly_Climatology/).
The MERRA-2 Project is accessible at the Global Modeling and Assimilation Office web site (https://gmao.gsfc.nasa.gov/reanalysis/MERRA-2/).

References

Abadie, C., Lacan, F., Radic, A., Pradoux, C., & Poitrasson, F. (2017), Iron isotopes reveal distinct dissolved iron sources and pathways in the intermediate versus deep Southern Ocean, *Proceedings of the National Academy of Sciences of the United States of America*, 114, 858–863. doi:10.1073/pnas.1603107114.

Archer, D. E., & Johnson, K. (2000), A Model of the iron cycle in the ocean, *Global Biogeochemical Cycles*, 14, No.1, 269-279, March.

Aumont, O., & Bopp, L. (2006), Globalizing results from ocean in situ iron fertilization studies, *Global Biogeochemical Cycles*, 20, GB2017, doi:10.1029/2005GB002591.

Aumont, O., Ethé, C., Tagliabue, A., Bopp, L., & Gehlen, M. (2015), PISCES-v2: An ocean biogeochemical model for carbon and ecosystem studies, *Geoscientific Model Development*, 8(8), 2465–2513, doi:10.5194/gmd-8-2465-2015.

Bennett, S. A., Achterberg, E. P., Connelly, D. P., Statham, P. J., Fones, G. R., & German, C. R. (2008), The distribution and stabilization of dissolved Fe in deep-sea hydrothermal plumes, *Earth and Planetary Science Letters*, 270, 157–167.

Blain, S., & Tagliabue, A. (2016), *Iron Cycle in Oceans*, Hoboken, NJ: John Wiley & Sons Incorporated.

Boiteau, R. M., Mende, D. R., Hawco, N. J., McIlvin, M. R., Fitzsimmons, J. N., Saito, M. A., et al. (2016), Siderophore-based microbial adaptations to iron scarcity across the eastern Pacific Ocean, *Proceedings of the National Academy of Sciences of the United States of America*, 113, 14237–14242, doi:10.1073/pnas.1608594113.

Bowie, A. R., & Lohan M. C. (2009), Determination of Iron in Seawater, in Wurl O., *Practical Guidelines for the Analysis of Seawater*, pp. 235–257, Boca Raton: CRC Press.

Brix, H., Menemenlis, D., Hill, C., Dutkiewicz, S., Jahn, O., Wang, D., et al. (2015), Using Green's Functions to initialize and adjust a global, eddying ocean biogeochemistry general circulation model, *Ocean Modelling*, 95, 1–14, doi:10.1016/j.ocemod.2015.07.008.

Chever, F., Bucciarelli, E., Sarthou, G., Speich, S., Arhan, M., Penven, P., & Tagliabue, A. (2010), Physical speciation of iron in the Atlantic sector of the Southern Ocean along a transect from the subtropical domain to the Weddell Sea Gyre, *Journal of Geophysical Research*, 115, C10059, doi:10.1029/2009JC005880.

Doi, T., Osafune, S., Sugiura, N., Kouketsu, S., Murata, A., Masuda, S., & Toyoda, T. (2015), Multidecadal change in the dissolved inorganic carbon in a long-term ocean state estimation, *Journal of Advances in Modeling Earth Systems*, 07, doi:10.1002/2015MS000462.

Doney, S. C., Lindsay, K., Fung, I., & John, J. (2006), Natural variability in a stable, 1000-yr global coupled climate-carbon cycle simulation, *Journal of Climate*, 19 (13), 3033–3054, doi:10.1175/JCLI3783.1.

Ellwood, M. J., Bowie, A. R., Baker, A., Gault-Ringold, M., Hassler, C., Law, C. S., et al. (2018), Insights Into the Biogeochemical Cycling of Iron, Nitrate, and Phosphate Across a 5,300 km South Pacific Zonal Section (153 degrees E-150 degrees W), *Global Biogeochemical Cycles*, 32, 187-207, doi:10.1002/2017GB005736.

Fitzsimmons, J. N., Carrasco, G. C., Wu, J. F., Roshan, S., Hatta, M., Measures, C. I., et al. (2015), Partitioning of dissolved iron and iron isotopes into soluble and colloidal phases along the GA03 GEOTRACES North Atlantic Transect. *Deep-Sea Research Part II-Topical Studies in Oceanography*, 116, 130-151, doi:10.1016/j.dsr2.2014.11.014.

Fitzsimmons, J. N., John, S. G., Marsay, C. M., Hoffman, C. L., Nicholas, S. L., Toner, B. M., et al. (2017), Iron persistence in a distal hydrothermal plume supported by dissolved–particulate exchange, *Nature Geoscience*, 10, 195–201, doi:10.1038/ngeo2900.

Frants, M., Holzer, M., DeVries, T., & Matear, R. (2016), Constraints on the global marine iron cycle from a simple inverse model, *Journal of Geophysical Research: Biogeosciences*, 121, 28–51, doi:10.1002/2015JG003111.

Gelaro, R., McCarty, W., Suárez, M. J., Todling, R., Molod, A., Takacs, L., et al. (2017), The Modern-Era Retrospective Analysis for Research and Applications, Version 2 (MERRA-2), *Journal of Climate*, 30, 5419–5454. https://doi.org/10.1175/JCLI-D-16-0758.1

German, C. R., Casciotti, K. A., Dutay, J. C., Heimburger, L. E., Jenkins, W. J., Measures, C. I., et al. (2016), Hydrothermal impacts on trace element and isotope ocean biogeochemistry. *Philosophical Transactions of the Royal Society A-Mathematical Physical and Engineering Sciences*, 374, 20160035, doi:10.1098/rsta.2016.0035.

Gregg, W. W., Ginoux, P., Schopf, P. S., & Casey, N. W. (2003), Phytoplankton and iron:

Validation of a global three-dimensional ocean biogeochemical model, *Deep-Sea Research Part II*, 50 (22–26), 3143–3169.

Hatta, M., Measures, C. I., Wu, J., Roshan, S., Fitzsimmons, J. N., Sedwick, P., & Morton, P. (2014), An overview of dissolved Fe and Mn Distributions during the 2010–2011 U.S. GEOTRACES north Atlantic Cruises: GEOTRACES GA03, *Deep Sea Research Part II: Topical Studies in Oceanography*, 116, 117–129, doi:10.1016/j.dsr2.2014.07.005.

Heller, M. I., Lam, P. J., Moffett, J. W., Till, C. P., Lee, J.-M., Toner, B. M., & Marcus, M. A. (2017), Accumulation of Fe oxyhydroxides in the Peruvian oxygen deficient zone implies non-oxygen dependent Fe oxidation, *Geochimica et Cosmochimica Acta*, 211, 174–193, doi:10.1016/j.gca.2017.05.019.

John, S. G., Helgoe, J., Townsend, E., Weber, T., DeVries, T., Tagliabue, A., et al. (2018), Biogeochemical cycling of Fe and Fe stable isotopes in the Eastern Tropical South Pacific, *Marine Chemistry*, 201, 66–76. doi:10.1016/j.marchem.2017.06.003.

Klunder, M. B., Laan, P., Middag, R., De Baar, H. J. W., & van Ooijen, J. C. (2011), Dissolved iron in the Southern Ocean (Atlantic sector), *Deep Sea Research Part II: Topical Studies in Oceanography*, 58, 2678–2694, doi:10.1016/j.dsr2.2010.10.042.

Klunder, M. B., Laan, P., De Baar, H. J. W., Neven, I., Middag, R., & Van Ooijen, J. (2013), Dissolved Fe across the Weddell Sea and Drake Passage: impact of DFe on nutrients uptake in the Weddell Sea, *Biogeosciences Discussions*, 10, 7433–7489, doi:10.5194/bgd-10-7433-2013.

Klunder, M. B., Bauch, D., Laan, P., de Baar, H. J. W., van Heuven, S., & Ober, S. (2012a), Dissolved iron in the Arctic shelf seas and surface waters of the central Arctic Ocean: Impact of Arctic river water and ice-melt, *Journal of Geophysical Research: Oceans*, 117, doi:10.1029/2011JC007133.

Klunder, M. B., Laan, P., Middag, R., de Baar, H. J. W., & Bakker, K. (2012b), Dissolved iron in the Arctic Ocean: Important role of hydrothermal sources, shelf input and scavenging removal, *Journal of Geophysical Research: Oceans*, 117, doi:10.1029/2011JC007135.

Kouketsu, S., Doi, T., Kawano, T., Masuda, S., Sugiura, N., Sasaki, Y., et al. (2011), Deep ocean heat content changes estimated from observation and reanalysis product and their influence on sea level change, *Journal of Geophysical Research: Oceans*, 116 (C3), doi:10.1029/2010JC006464.

Lacan, F., Radic, A., Jeandel, C., Poitrasson, F., Sarthou, G., Pradoux, C., & Freydier, R. (2008), Measurement of the isotopic composition of dissolved iron in the open ocean, *Geophysical Research Letters*, 35, L24610, doi:10.1029/2008GL035841.

Luo, C., Mahowald, N. M., & Del Corral, J. (2003), Sensitivity study of meteorological parameters on mineral aerosol mobilization, transport, and distribution, *Journal of Geophysical Research: Atmospheres*, 108 (D15), 4447, doi:10.1029/2003JD003483.

Masuda, S., Awaji, T., Sugiura, N., Matthews, J. P., Toyoda, T., Kawai, Y., et al. (2010), Simulated Rapid Warming of Abyssal North Pacific Waters, *Science*, 329, 319–322.

McClain, C. R., Cleave, M. L., Feldman, G. C., Gregg, W. W., Hooker, S. B., & Kuring, N. (1998), Science quality SeaWiFS data for global biosphere research, *Sea Technology September*, 10–16.

Menemenlis, D., Fukumori, I., & Lee, T. (2005), Using Green's functions to calibrate an ocean general circulation model, *Monthly Weather Review*, 133, 1224–1240.

Minami, T., Konagaya, W., Zheng, L., Takano, S., Sasaki, M., Murata, R., et al. (2015), An off-line automated preconcentration system with ethylenediaminetriacetate chelating resin for the determination of trace metals in seawater by high-resolution inductively coupled plasma mass spectrometry, *Analytica Chimica Acta*, 854, 183–190. doi:10.1016/j.aca.2014.11.016.

Misumi, K., Tsumune, D., Yoshida, Y., Uchimoto, K., Nakamura, T., Nishioka, J., et al. (2011), Mechanisms controlling dissolved iron distribution in the North Pacific: A model study, *Journal of Geophysical Research: Biogeosciences*, 116, G03005, doi:10.1029/2010JG001541.

Misumi, K., Lindsay, K., Moore, J. K., Doney, S. C., Bryan, F. O., Tsumune, D., & Yoshida, Y. (2014), The iron budget in ocean surface waters in the 20th and 21st centuries: projections by the Community Earth System Model version 1, *Biogeosciences*, 11, 33–55, doi:10.5194/bg-11-33-2014.

Moore, J. K., Doney, S. C., & Lindsay, K. (2004), Upper ocean ecosystem dynamics and iron cycling in a global three-dimensional model, *Global Biogeochemical Cycles*, 18, GB4028, doi:10.1029/2004GB002220.

Moore, J. K., & Braucher, O. (2008), Sedimentary and mineral dust sources of dissolved iron to the world ocean, *Biogeosciences*, 5 (3), 631–656, doi:10.5194/bg-5-631-2008.

Nishioka, J., Obata, H., & Tsumune, D. (2013), Evidence of an extensive spread of hydrothermal dissolved iron in the Indian Ocean. *Earth and Planetary Science Letters*, 361, 26–33, doi:10.1016/j.epsl.2012.11.040.

Nishioka, J., & Obata, H. (2017), Dissolved iron distribution in the western and central subarctic Pacific: HNLC water formation and biogeochemical processes. *Limnology and Oceanography*, 62, 2004–2022, doi:10.1002/lno.10548.

Nishioka, J., Obata, H., Ogawa, H., Ono, K., Yamashita, Y., Lee, K. J., et al. (2020), Subpolar marginal seas fuel the North Pacific through the intermediate water at the termination of the global ocean circulation, *Proceedings of the National Academy of Sciences*, https://doi.org/10.1073/pnas.2000658117.

Osafune, S., Masuda, S., Sugiura, N., & Doi, T. (2015), Evaluation of the applicability of the Estimated State of the Global Ocean for Climate Research (ESTOC) data set, *Geophysical Research Letters*, 42, 4903–4911, doi:10.1002/2015GL064538.

Pacanowski, R. C., & Griffies, S. M. (1999), The MOM 3 manual, report, 680 pp, Geophys. Fluid Dyn. Lab., Princeton, N. J.

Resing, J. A., Sedwick, P. N., German, C. R., Jenkins, W., Moffett, J. W., Sohst, B., & Tagliabue, A. (2015), Basin-scale transport of hydrothermal dissolved metals across the South Pacific Ocean, *Nature*, doi:10.1038/nature14577.

Rijkenberg, M. J. A., Middag, R., Laan, P., Gerringa, L. J. A., van Aken, H. M., Schoemann, V., et al. (2014), The distribution of dissolved iron in the west Atlantic Ocean, *PloS One*, 9, e101323, doi:10.1371/journal.pone.0101323.

Romankevich, E. (1977), Analysis of data on organic carbon in seawater and suspension. The balance of carbon in the world ocean, *Geochemistry of Organic Matter in the Ocean*, 1–304, Springer-Verlag, Berlin.

Saito, M. A., Noble, A. E., Tagliabue, A., Goepfert, T. J., Lamborg, C. H., & Jenkins, W. J. (2013), Slow-spreading submarine ridges in the South Atlantic as a significant oceanic iron source, *Nature Geoscience*, 6, 775–779, doi:10.1038/NGEO1893.

Sanial, V., Kipp, L. E., Henderson, P. B., van Beek, P., Reyss, J.-L., Hammond, D. E., et al. (2018), Radium-228 as a tracer of dissolved trace element inputs from the Peruvian continental margin. *Marine Chemistry*, 201, 20–34, doi:10.1016/j.marchem.2017.05.008.

Schlitzer, R., Anderson, R. F., Masferrer Dodas, E., Lohan, M., Geibert, W., Tagliabue, A., et al. (2018), The GEOTRACES Intermediate Data Product 2017, *Chemical Geology*. https://doi.org/10.1016/j.chemgeo.2018.05.040

Schmittner, A., Oschlies, A., Matthews, H. D., & Galbraith, E. D. (2008), Future changes in climate, ocean circulation, ecosystems, and biogeochemical cycling simulated for a business-as-usual CO_2 emission scenario until year 4000 AD, *Global Biogeochemical Cycles*, 22, GB1013, doi:10.1029/2007GB002953.

Smith Jr., K. L., Robison, B. H., Helly, J. J., Kaufmann, R. S., Ruhl, H. A., Shaw, T. J., et al. (2007), Free-drifting icebergs: Hot spots of chemical and biological enrichment in the Weddell Sea, *Science*, 317, 478–482.

Tagliabue, A., Bopp, L., Dutay, J., Bowie, A., Chever, F., Jean-Baptiste, P., et al. (2010), Hydrothermal contribution to the oceanic dissolved iron inventory, *Nature Geoscience*, 3, 252-256, https://doi.org/10.1038/ngeo818.

Tagliabue, A., Mtshali, T., Aumont, O., Bowie, A.R., Klunder, M.B., Roychoudhury, A.N., & Swart, S. (2012), A global compilation of dissolved iron measurements: focus on distributions and processes in the Southern Ocean, *Biogeosciences*, 9, 2333-2349, https://doi.org/10.5194/bg-9-2333-2012.

Tagliabue, A., Aumont, O., DeAth, R., Dunne, J. P., Dutkiewicz, S., Galbraith, E., et al. (2016), How well do global ocean biogeochemistry models simulate dissolved iron distributions?, *Global Biogeochemical Cycles*, 30, doi:10.1002/2015GB005289.

Tagliabue, A., Bowie, A. R., Boyd, P. W., Buck, K. N., Johnson, K. S., & Saito, M. A. (2017),

The integral role of iron in ocean biogeochemistry, *Nature*, 543, 51–59.

Toyoda, T., Awaji, T., Masuda, S., Sugiura, N., Igarashi, H., Sasaki, Y., et al. (2013), Improved state estimations of lower trophic ecosystems in the global ocean based on a Green's function approach, *Progress in Oceanography*, 119, 90–107.

Toyoda, T., Sugiura, N., Masuda, S., Sasaki, Y., Igarashi, H., Ishikawa, Y., et al. (2015), An improved simulation of the deep Pacific Ocean using optimally estimated vertical diffusivity based on the Green's function method, *Geophysical Research Letters*, 42, 9916–9924, doi:10.1002/2015GL065940.

Vu, H. T. D., & Sohrin, Y. (2013), Diverse stoichiometry of dissolved trace metals in the Indian Ocean, *Scientific Reports*, 3, 1745, doi:10.1038/srep01745.

Yamashita, Y., Nishioka, J., Obata, H., & Ogawa, H. (2020), Shelf humic substances as carriers for basin-scale iron transport in the North Pacific, *Scientific Reports*, 10, 4505, doi:10.1038/s41598-020-61375-7.

Zheng, L., Minami, T., Takano, S., Minami, H., & Sohrin, Y. (2017), Distribution and stoichiometry of Al, Mn, Fe, Co, Ni, Cu, Zn, Cd, and Pb in seawater around the Juan de Fuca Ridge, *Journal of Oceanography*, 73, 669-685, doi:10.1007/s10872-017-0424-2.